How to cite: *Angew. Chem. Int. Ed.* **2021**, *60*, 20331 – 20341
International Edition: doi.org/10.1002/anie.202104918
German Edition: doi.org/10.1002/ange.202104918

Nitrogen Reduction Catalysts

Identification of M-NH_2-NH_2 Intermediate and Rate Determining Step for Nitrogen Reduction with Bioinspired Sulfur-Bonded FeW Catalyst

Yilong Zhao[+], Fusheng Li[+], Wenlong Li, Yingzheng Li, Chang Liu, Ziqi Zhao, Yu Shan, Yongfei Ji, and Licheng Sun**

Abstract: *The multimetallic sulfur-framework catalytic site of biological nitrogenases allows the efficient conversion of dinitrogen (N_2) to ammonia (NH_3) under ambient conditions. Inspired by biological nitrogenases, a bimetallic sulfide material ($FeWS_x$@$FeWO_4$) was synthesized as a highly efficient N_2 reduction (NRR) catalyst by sulfur substitution of the surface of $FeWO_4$ nanoparticles. Thus prepared FeW-S_x@$FeWO_4$ catalysts exhibit a relatively high NH_3 production rate of 30.2 ug h^{-1} mg^{-1}_{cat} and a Faraday efficiency of 16.4 % at −0.45 V versus a reversible hydrogen electrode in a flow cell; these results have been confirmed via purified $^{15}N_2$-isotopic labeling experiments. In situ Raman spectra and hydrazine reduction kinetics analysis revealed that the reduction of undissociated hydrazine intermediates (M-NH_2-NH_2) on the surface of the bimetallic sulfide catalyst is the rate-determing step for the NRR process. Therefore, this work can provide guidance for elucidating the structure–activity relationship of NRR catalysts.*

Introduction

Ammonia (NH_3) is one of the most important feedstocks for industries and also a promising energy carrier for future renewable energy technologies.[1,2] Compared with the strategic alternatives for the capital- and energy-intensive Haber-Bosch process, photocatalytic and electrocatalytic approaches are regarded as environmentally benign and energy-saving processes for NH_3 production, since they can be performed using renewable energies (such as solar and wind power) under ambient conditions.[3–6] However, as a non-polar diatomic molecule, dinitrogen (N_2) possesses a strong homonuclear triple bond (941 kJ mol^{-1}) and is inert toward direct hydrogenation,[7,8] thereby, leading to sluggish kinetics of photocatalytic and electrocatalytic nitrogen reduction reactions (NRRs) and a competition for the hydrogen evolution reaction (HER).[9–11]

Thus far, homogenous molecular NRR catalysts based on molybdenum, iron, and titanium complexes have been proposed for the reduction of N_2 to NH_3 under ambient conditions; however, their stability and recycling issues have not been satisfactorily addressed.[12–15] Heterogeneous NRR catalysts based on transition metal oxides, sulfides, and single atomic catalysts have attracted significant attention; however, the pursuit of efficient heterogeneous NRR catalysts with high NH_3 production rates and high Faraday efficiencies (FEs) remains challenging.[16–18] On the other hand, a comprehensive understanding of nitrogen hydrogenation processes is vital for fabricating efficient artificial NRR catalysts. Significant efforts have been devoted to study the hydrogenation process of NRR catalysts, but the available reports on the nitrogen hydrogenation mechanism of artificial NRR catalysts still rely on theoretical calculations and lack experimental investigations.[19,20]

In nature, N_2-fixing nitrogenases are a cascade of enzymes in azotobacters that catalyze the reduction of N_2 and H^+ to produce NH_3 and H_2.[21] Nitrogenases commonly comprise a metallic sulfur framework in the charge-transfer protein (Fe protein) and multimetal N_2-fixing protein (MoFe-, VFe- or FeFe- cofactors), which is remarkably efficient for NRRs in aqueous environments and at room temperature.[21,22] However, there is insignificant information about the pathway and intermediates involved in N_2 reduction by nitrogenases. Early studies revealed the existence of a bound intermediate at the level of reduction of hydrazine (H_2N-NH_2) for MoFe

[*] Y. Zhao,[+] F. Li,[+] W. Li, Y. Li, C. Liu, Z. Zhao, Y. Shan, L. Sun
State Key Laboratory of Fine Chemicals, Institute of Artificial Photosynthesis, DUT-KTH Joint Education and Research Centre on Molecular Devices, Dalian University of Technology
Dalian 116024 (P. R. China)
E-mail: fusheng@dlut.edu.cn
L. Sun
Department of Chemistry, School of Engineering Sciences in Chemistry, Biotechnology and Health, KTH Royal Institute of Technology
10044 Stockholm (Sweden)
and
Center of Artificial Photosynthesis for Solar Fuels, School of Science, Westlake University
Hangzhou 310024 (China)
E-mail: sunlicheng@westlake.edu.cn
Y. Ji
School of Chemistry and Chemical Engineering, Guangzhou University
Guangzhou 510006 (China)
[+] These authors contributed equally to this work.
Supporting information and the ORCID identification number(s) for the author(s) of this article can be found under: https://doi.org/10.1002/anie.202104918.

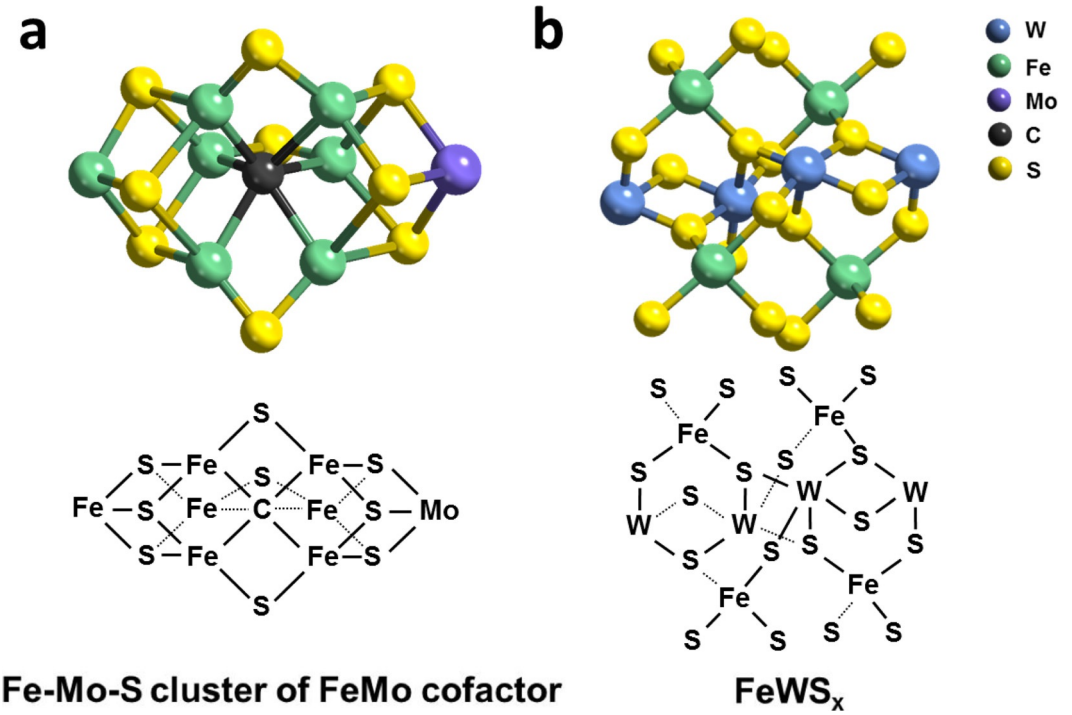

Scheme 1. Structure of a) the Fe-Mo-S cluster of FeMo cofactor in nitrogenase[21] and b) the synthetic $FeWS_x$ on the surface of $FeWS_x$@$FeWO_4$ NPs.

cofactors during the reaction.[23] Meanwhile, several logical assumptions have been proposed, and two classes of reduction pathways have been widely accepted and are distinguished by the site of hydrogenation on bound N-N fragments.[24–26] 1) The distal pathway: N_2 is hydrogenated at a single (distal) N atom until the N–N bond is cleaved with the release of the first NH_3, which is followed by NH_3 released by further reduction of the bound nitrido species.[25,26] 2) The alternating pathway: the two N atoms of N_2 are reduced alternately, with the N–N bond cleavage occurring only later in the reaction.[25,26] The structure of bimetallic cofactors (Scheme 1 a) may provide a template for the design of efficient artificial NRR catalysts and a mechanistic understanding of nitrogen hydrogenation processes. The synergistic effect of the bimetallic sites of the N_2-fixing protein has advantages in polarizing and activating the strong non-polar triple bond of N_2, and facilitating the protonation processes.[27,28] The protein scaffold provides a beneficial secondary coordination sphere comprising H-bonding and redox-active moieties, which regulate the proton-coupled electron transfer steps for minimal H_2 production.[29]

Herein, inspired by the bimetallic sulfur architectures of the N_2-fixing cofactors, an iron and tungsten bimetallic sulfide catalyst ($FeWS_x$@$FeWO_4$, Scheme 1 b) was synthesized by sulfur substitution of the surface of $FeWO_4$ nanoparticles. Nitrogen temperature-programmed desorption (N_2-TPD) results demonstrate that $FeWS_x$@$FeWO_4$ exhibited better nitrogen adsorption capability when sulfur gradually replaced the oxygen on the $FeWO_4$ surface. The potential of NRR shifted from −0.65 V to −0.45 V versus reversible hydrogen electrode (RHE), and the FE increased from 0.89 % to 6.01 % in the H-type cell. When the mass transfer on the surface of the catalyst was greatly improved by the application of a flow cell and gas diffusion electrodes, a boosted FE of 16.4 %, and a maintained NH_3 yield of 30.2 $ug\,h^{-1}\,mg^{-1}_{cat}$ quantified with $^{15}N_2$ can be obtained under ambient conditions. The in situ Raman spectra and analysis of hydrazine reduction kinetics confirmed that the reduction of intermediates with a metal-hydrazine structure plays an important role in the NRR rate for the bimetallic sulfide catalysts. This work provides a new perspective for enhancing NRR catalytic activity by introducing bimetallic sulfide bonds on the surface of catalysts.

Results and Discussion

Preparation and characterization of $FeWS_x$@$FeWO_4$

As illustrated in Figure 1 a, $FeWS_x$@$FeWO_4$ nanoparticles (NPs) were synthesized using a two-step fabrication strategy. $FeWO_4$ NPs were first prepared by a hydrothermal reaction according to a previously reported method.[30] Then, the surface oxygen of the $FeWO_4$ NPs was replaced by sulfur atoms through sulfur substitution at 450 °C under an argon atmosphere. The vulcanization process was performed with different equivalents of sulfur powder, namely: single, double, and quadruple weights of the $FeWO_4$ NPs; the resulting catalysts were named $FeWS_x$@$FeWO_4$-1, $FeWS_x$@$FeWO_4$-2, and $FeWS_x$@$FeWO_4$-4, respectively. No nitrogen-containing compounds were used as reactants or other reagents for the catalyst preparation.

The morphologies, compositions, and oxidation states of the prepared $FeWS_x$@$FeWO_4$ and $FeWO_4$ were characterized using scanning electron microscopy (SEM), transmission

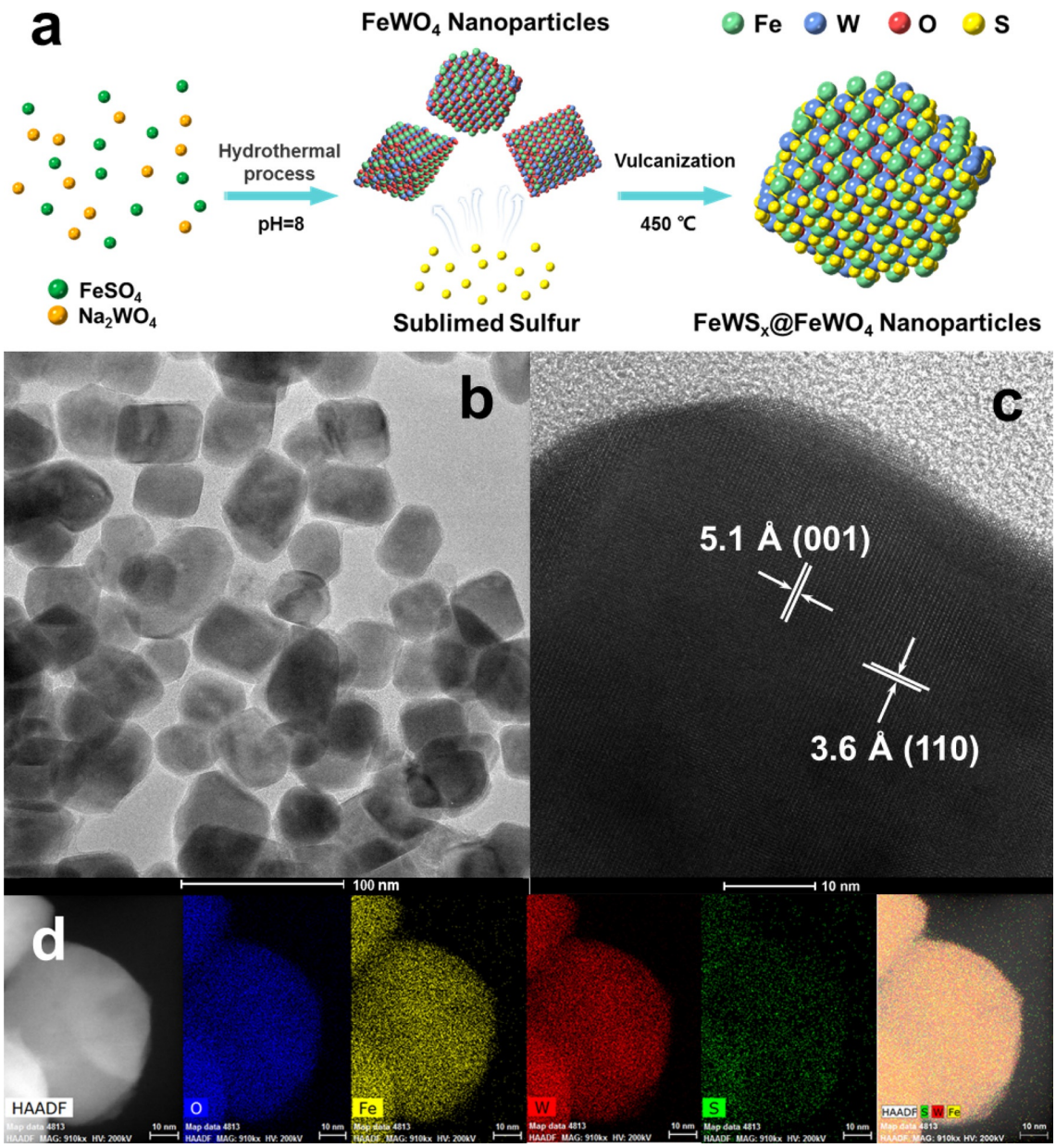

Figure 1. a) Schematic diagram of the synthetic procedure of $FeWS_x$@$FeWO_4$ nanoparticles (NPs). b) TEM, and c) HRTEM images of $FeWS_x$@$FeWO_4$-2 NPs. d) HAADF-STEM and the corresponding EDX elemental mappings for $FeWS_x$@$FeWO_4$-2 NPs.

electron microscopy (TEM), X-ray powder diffraction (XRD), Raman spectroscopy, Fourier transform infrared analysis (FT-IR), and X-ray photoelectron spectroscopy (XPS). After vulcanization, the color of $FeWO_4$ changed from brown to dark, which indicated anion exchange on the surface of $FeWO_4$ NPs by the vulcanization process (Figure S1). SEM analysis showed that the $FeWS_x$@$FeWO_4$ catalysts retained their morphology as $FeWO_4$ NPs, and excess sulfur was observed on the surface of $FeWS_x$@$FeWO_4$-4. The diameter of the representative sample of $FeWS_x$@$FeWO_4$-2 was approximately 50 ± 10 nm, according to the TEM image (Figure 1b). The high-resolution TEM image (Figure 1c) shows lattice fringes of crystalline species with typical d-spacings of 5.1 Å and 3.6 Å, corresponding to the (001) and (110) crystal planes of the $FeWO_4$ core of the $FeWS_x$@$FeWO_4$-2 catalyst, respectively.[31,32] The lattice fringes exhibit distortion in the border area of the $FeWS_x$@$FeWO_4$-2 NPs (Figure S2), indicating the sulfur atoms have replaced the oxygen on the surface of $FeWO_4$.[33] The TEM images of the other catalysts are shown in Figure S3. More sulfur flakes are on the surface of $FeWS_x$@$FeWO_4$-4, which is consistent with the SEM results. High-angle annular dark-field scanning transmission electron microscopy (HAADF-STEM) corresponding to energy-dispersive X-ray spectroscopy (EDS) elemental mapping shows the distribution of Fe, W, S, and O in the $FeWS_x$@$FeWO_4$ nanoparticles (Figure 1d). The Fe and W elements are gradually dispersed from the center to the edge of the NPs. Oxygen is mainly

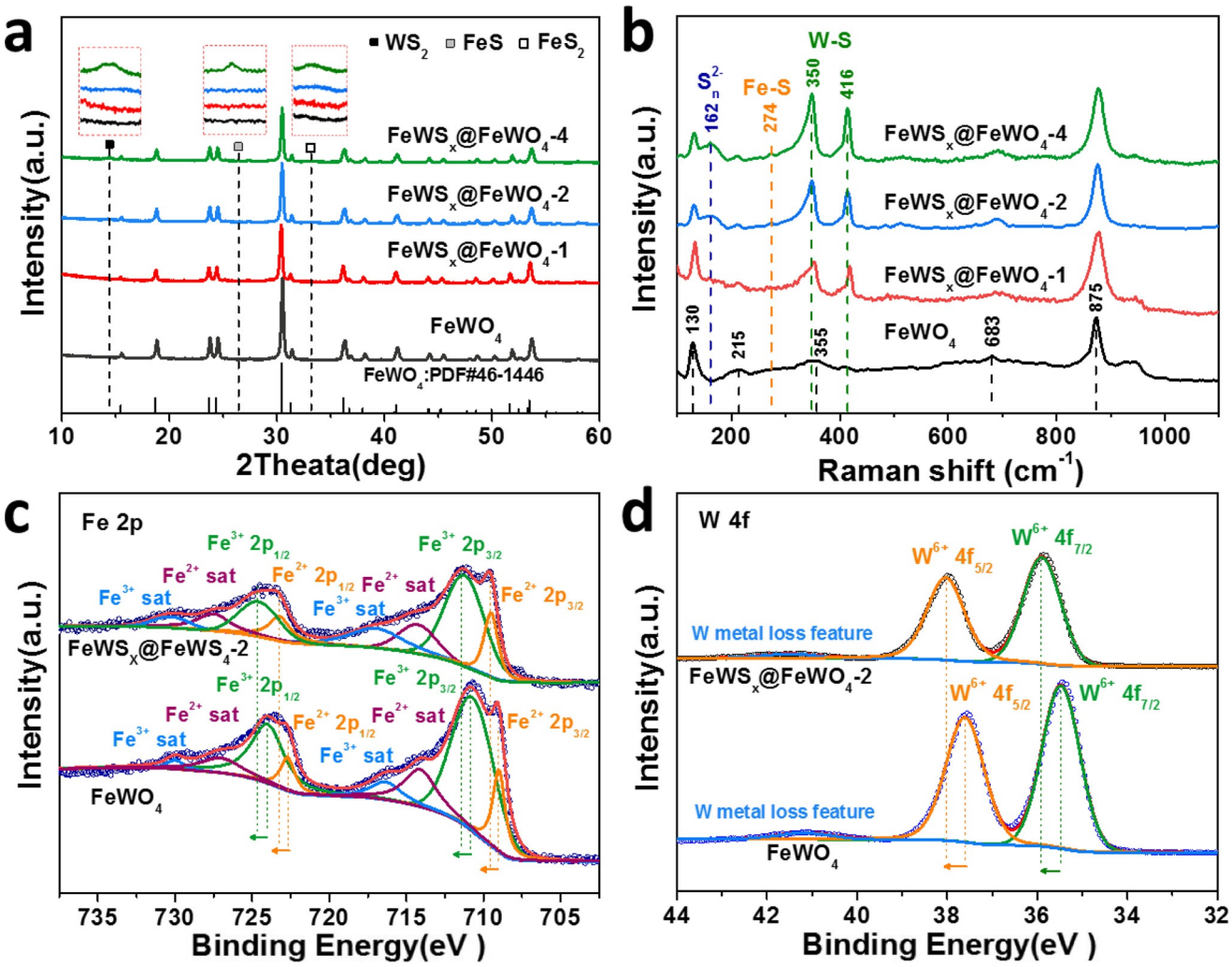

Figure 2. a) XRD pattern and b) Raman spectra of $FeWO_4$ and $FeWS_x$@$FeWO_4$ NPs. XPS of c) Fe 2p and d) W 4f for $FeWO_4$ and $FeWS_x$@$FeWO_4$-2 NPs.

distributed in the core region; however, S is located at the surface of the catalyst. These EDS elemental mapping images indicate that the oxygen atoms on the surface of $FeWO_4$ were successfully replaced by sulfur after the vulcanization process.

The XRD patterns of the $FeWS_x$@$FeWO_4$ catalysts and $FeWO_4$ are displayed in Figure 2a. The diffraction peaks at 18.8°, 30.5°, 36.3°, 41.2°, and 53.7° for $FeWS_x$@$FeWO_4$-1, $FeWS_x$@$FeWO_4$-2, and $FeWO_4$ can be assigned to the (100), (111), (021), (121), and (221) lattice planes of $FeWO_4$ indexed to the orthorhombic system of PDF#46-1446 (without impurity peaks),[34] respectively. This indicates that the crystal structure of the $FeWO_4$ core is maintained after appropriate vulcanization. When the XRD spectra were enlarged, it was found that the diffraction peaks of (100) and (111) planes were slightly shifted after vulcanization (Figure S4). However, three faint diffraction peaks at 14.3°, 26.4°, and 33.0° were detected for $FeWS_x$@$FeWO_4$-4, corresponding the (002) facet of WS_2,[35] (220) facet of FeS, and (101) facet of FeS_2, respectively;[36] these results suggested that excessive vulcanization could destroy the main structure of $FeWO_4$.

The Raman spectra (Figure 2b) of the $FeWO_4$ NPs exhibit characteristic peaks at 130, 215, 355, 683, and 875 cm^{-1}, which are consistent with previous reports.[37,38] After vulcanization, the new Raman peaks assigned to the variations of S_n^{2-} (162 cm^{-1}),[39] Fe-S (274 cm^{-1}),[40] and W-S (350 and 416 cm^{-1})[41] were observed for the $FeWS_x$@$FeWO_4$-1, $FeWS_x$@$FeWO_4$-2, and $FeWS_x$@$FeWO_4$-4 catalysts, and the intensity of these Raman peaks gradually increased with the increase in the equivalents of sulfur in the vulcanization process. As shown in the FT-IR spectra (Figure S5), the classic bands of $FeWO_4$ can be detected at 508, 650, and 854 cm^{-1}, corresponding to the symmetric vibration of Fe-W-O, stretching vibration of W-O, and asymmetric deformation vibration of Fe-O, respectively.[42] The antisymmetric (1390 cm^{-1}) and symmetrical stretching vibration bands (1141 cm^{-1}) of sulfoxide (S−O/S=O) were detected on the surface of $FeWS_x$@$FeWO_4$-2.[43,44] Meanwhile, the stretching vibration absorption of S−O/S=O was also observed at 1091 and 1045 cm^{-1}.[43] After further vulcanization, more stretching vibration bands of S=O were observed at 1402, 1195, and 1117 cm^{-1} for the $FeWS_x$@$FeWO_4$-4 catalyst.[45–47]

The elemental composition and the corresponding valence states were further analyzed by XPS (Figure S6). According to standard deconvolution principles, the Fe 2p high-resolution XPS spectrum of $FeWO_4$ was divided into four sets of peaks attributed to the states of Fe^{2+} (722.7 eV and 709.1 eV) and Fe^{3+} (724.1 eV and 710.8 eV), and their satellites (730.0 eV, 727.1 eV, 716.4 eV, and 714.1 eV, respectively) (Figure 2c).[48] The peak position analysis of the W 4f orbital indicated the presence of valence states of +6 for W ($4f_{5/2}$, 37.6 eV, and $4f_{7/2}$, 35.5 eV) (Figure 2d).[34] For the appropriate vulcanized sample ($FeWS_x$@$FeWO_4$-2), the binding energies at 163.5 eV and 162.3 eV were observed, corresponding to the S $2p_{1/2}$ and S $2p_{3/2}$ orbitals, respectively (Figure S7a); this result suggested the existence of disulfide anions linked with Fe or W metals.[40,49] Meanwhile, species with higher binding energy between 169 and 171 eV were observed on the surface of the catalyst. Combined with the corresponding O 1s spectrum (Figure S7b), it can be concluded that S–O/S=O bonds exist on the surface of the vulcanized sample,[42] which is consistent with the corresponding FT-IR spectrum (Figure S5). Because of the presence of sulfur-oxygen bonds, which are strong electron-withdrawing groups, the binding energies of Fe and W in $FeWS_x$@$FeWO_4$-2 positively shifted; this is beneficial for promoting the interactions between N_2 and the catalyst and enhancing the NRR.[50] However, for the excessive vulcanized sample ($FeWS_x$@$FeWO_4$-4), owing to the reducibility of sulfur, the binding energies of metallic state Fe^0 (721.1 eV and 708.0 eV) and W^{4+} (34.7 eV and 32.7 eV) were observed in FeW-S_x@$FeWO_4$-4 NPs (Figure S7c and S7d).[42,51]

The characterization of the synthesized catalysts can be summarized as follows: 1) After vulcanization, oxygen atoms on the surface of $FeWO_4$ NPs can be successfully substituted by sulfur. 2) Strong electron-withdrawing sulfur-oxygen bonds exist on the surface of $FeWS_x$@$FeWO_4$, which is beneficial for NRRs. 3) Excessive vulcanization can destroy the main structure of $FeWO_4$; sulfur flakes will be deposited on the surface of the catalyst, and the cations of $FeWO_4$ can be reduced.

Electroreduction of N_2 to NH_3

The electrochemically active surface area (ECSA) of $FeWO_4$/CFP, $FeWS_x$@$FeWO_4$-1/CFP, $FeWS_x$@$FeWO_4$-2/CFP and $FeWS_x$@$FeWO_4$-4/CFP electrodes were measured (Figure S8), the ECSA could be increased after vulcanization. To investigate the effects of the conversion of bimetallic oxides to sulfides on the performance of the NRR, the electrocatalytic nitrogen reduction activities of the $FeWO_4$ and $FeWS_x$@$FeWO_4$ catalysts were measured in an enclosed H-type electrolytic cell (Figure S9). A high-purity N_2 gas (99.999%) was purged sequentially through a Cu-based impurity trap and a liquid-nitrogen-cooled trap to capture impurities such as NO_x and residual NH_3 according to the prevailing pre-treatment method.[52] The working electrodes were prepared by depositing 1 mg of catalyst onto carbon fiber paper (CFP) with the assistance of Nafion. The linear sweep voltammetry (LSV) curves of the $FeWO_4$ and FeW-S_x@$FeWO_4$ catalysts show increased responses for current density by changing the atmosphere of argon to N_2 (Figures S10 and S11), indicating that nitrogen reduction occurs by the catalysis of these catalysts. When replacing argon with N_2, the current increase started from −0.5 V versus RHE for the $FeWO_4$ catalyst (Figure S10a). However, after vulcanization, the current raising potentials of the NRR positively shifted with 0.1 and 0.2 V for $FeWS_x$@$FeWO_4$-1 and $FeWS_x$@$FeWO_4$-2 (Figures S10b, S10c and S11), respectively. This indicates that the transformation of bimetal active sites from oxides to sulfides and the introduction of strong electron-withdrawing sulfur-oxygen bonds on the surface of the catalyst can effectively reduce the potential required for the NRR, which is in agreement with XPS results. For $FeWS_x$@$FeWO_4$-4 (Figure S10d), the NRR potential cannot be further positively shifted by excessive vulcanization.

For the quantitative assessment of electrochemical NH_3 production, chronoamperometry measurements at different potentials (Figure S12) and UV/Vis absorption spectrometry analysis by an indophenol blue spectrophotometric method were performed, while the potential by-product of hydrazine was evaluated using the Watt and Chrisp approach (Figures S13, S14).[53,54] The NH_3 production rates (r_{NH_3}) and FEs of the $FeWO_4$ and $FeWS_x$@$FeWO_4$ catalysts are shown in Figure 3a–d. $FeWO_4$ exhibited the highest r_{NH_3} and FE of 12.26 $ug\,h^{-1}\,mg^{-1}_{cat}$ and 0.89% at −0.65 V (versus RHE) (Figure 3a). After vulcanization (Figure 3b and 3c), the highest activity potential of $FeWS_x$@$FeWO_4$-1 and FeW-S_x@$FeWO_4$-2 shifted positively, which is consistent with the LSV results. The r_{NH3} of $FeWS_x$@$FeWO_4$-1 increased to 13.19 $ug\,h^{-1}\,mg^{-1}_{cat}$ at −0.55 V with a FE of 1.5%, and the $FeWS_x$@$FeWO_4$-2 catalyst achieved the highest r_{NH_3} of 16.6 $ug\,h^{-1}\,mg^{-1}_{cat}$ at −0.45 V with an improved FE of 6.01%. For the excessively vulcanized $FeWS_x$@$FeWO_4$-4 catalyst, the highest activity potential is the same as FeW-S_x@$FeWO_4$-2 (−0.45 V versus RHE), while the highest r_{NH_3} (12.88 $ug\,h^{-1}\,mg^{-1}_{cat}$) and FE (2.2%) are both lower than those of $FeWS_x$@$FeWO_4$-2, indicating that the iron sulfide and tungsten sulfide phases generated by excessive vulcanization may be more conducive to the hydrogen evolution reaction (HER) rather than the NRR.

For the three-phase electrocatalytic reaction, the diffusion of reactants and electrolytes to the electrode surface is vital for the reaction rate, as nitrogen exhibits poor solubility in water.[55] In order to further improve the efficiency of the NRR, 1 mg of the $FeWS_x$@$FeWO_4$-2 catalyst was deposited on a gas diffusion electrode (gas diffusion layer, GDL, 1 cm^2), and the performance was re-measured in a flow cell (Figures 4a and S15). The hydrophobicity of the gas diffusion electrode and the serpentine gas transmission channel greatly promote the diffusion of the gas reactants on the electrode surface.[56] The r_{NH3} and FE of the $FeWS_x$@$FeWO_4$-2 catalyst in the flow cell were calibrated using ^1H nuclear magnetic resonance (NMR) spectroscopy (Figures 4b, S16 and S19a) and the indophenol blue method (Figures 4b and S17). After improving the nitrogen mass transfer on the electrode surface, the ammonia production yield of $FeWS_x$@$FeWO_4$-2 was significantly improved. A volcano shape with the highest

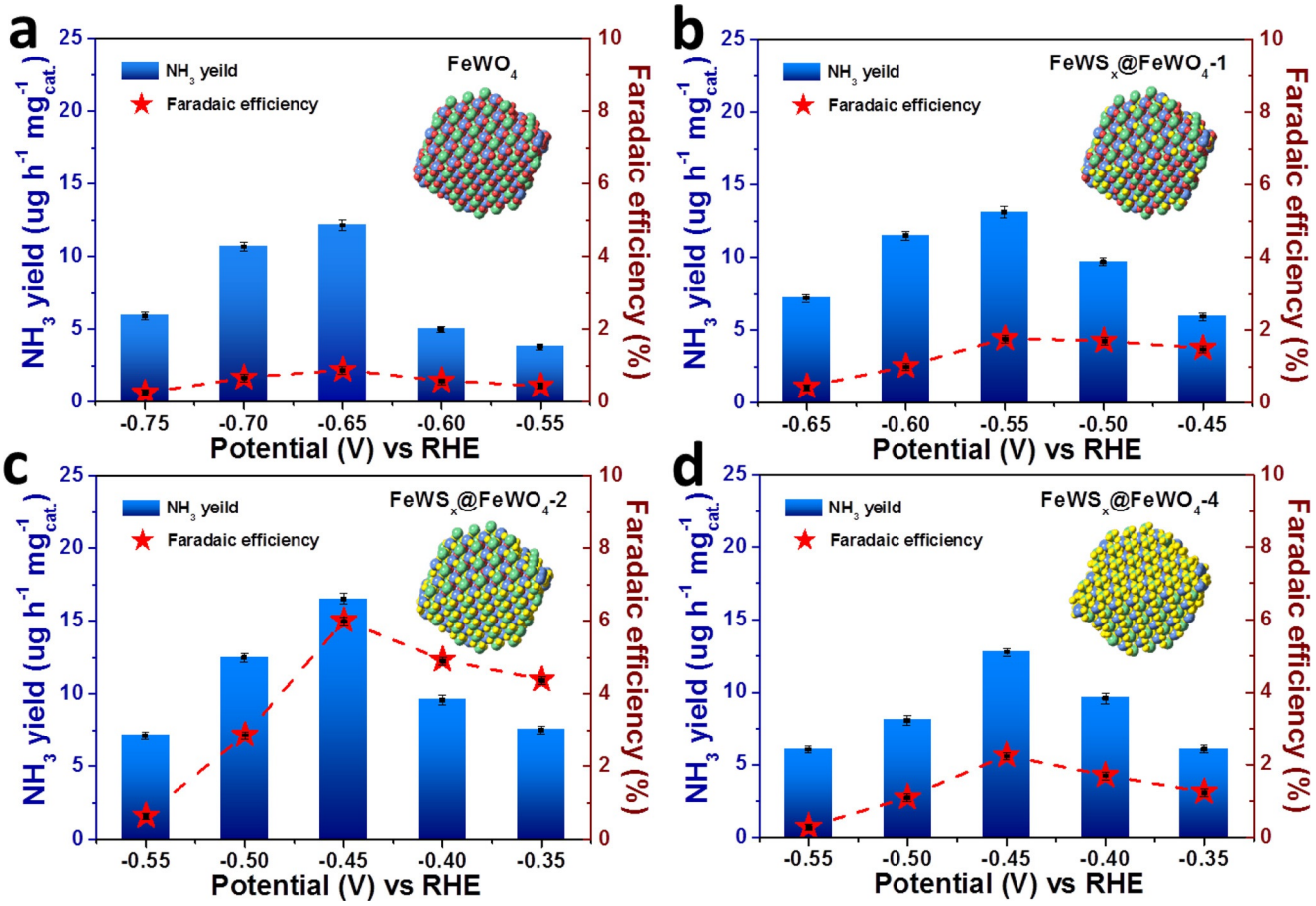

Figure 3. Ammonia yield and Faraday efficiency of a) $FeWO_4$, b) $FeWS_x$@$FeWO_4$-1, c) $FeWS_x$@$FeWO_4$-2 and d) $FeWS_x$@$FeWO_4$-4 under different potentials.

r_{NH_3} of 32.7 $ug\,h^{-1}\,mg^{-1}_{cat}$ and a maximum FE of 18.1% at −0.45 V was obtained (Figure 4b).

To further confirm the N source of NH_3 production, isotope labeling experiments using adequately cleaned $^{15}N_2$ as the feeding gas was conducted (Figure S18).[57] The chronoamperometry curves of $FeWS_x$@$FeWO_4$-2 at the corresponding potentials in the flow cell for 1 h are displayed in Figure S19b. As a reference, the standard ^1H NMR spectra of $^{15}NH_4Cl$ were recorded (Figure S20). The ^1H NMR spectra of the electrolyte (Figure 4c) and the gas absorption liquid (Figure 4d) after electrolysis were obtained using $^{15}N_2$ as the feeding gas for the $FeWS_x$@$FeWO_4$-2 catalyst; these spectra displayed a distinguishable doublet with a coupling constant of 73 Hz, which matched well with the standard for $^{15}NH_4^+$, thereby strongly supporting the fact that the generation of NH_3 is fed by N_2 and that no nitrogen pollution was introduced.[52] The highest $^{15}NH_4^+$ generation rate was 30.2 $ug\,h^{-1}\,mg^{-1}_{cat}$ at −0.45 V (versus RHE) with a maximum FE of 16.4% (Figure 4b). These data are consistent with the above-demonstrated results using $^{14}N_2$ as the feeding gas, indicating that sustainable NH_3 production is achieved by consuming N_2 supply.

Negligible NH_3 production was observed (Figure S21) under the following conditions: (i) KOH electrolyte; (ii) $FeWS_x$@$FeWO_4$-2 catalyst at −0.45 V in the Ar-fed electrolyte after 1 h electrolysis; (iii) sulfur-powder-modified CFP at −0.45 V in the $^{15}N_2$-fed electrolyte after 1 h electrolysis; (iv) CFP substrate at −0.45 V in the $^{15}N_2$-fed electrolyte after 1 h electrolysis; and (v) $FeWS_x$@$FeWO_4$-2 catalyst under open-circuit conditions in the $^{15}N_2$-fed electrolyte. These additional controlled experiments exclude the contribution of the contaminants to NH_3.

The stability of the $FeWS_x$@$FeWO_4$-2 catalyst was evaluated via cycling and chronoamperometric tests. As shown in Figure S22, after five tests, r_{NH3} was determined to be 27.3 $ug\,h^{-1}\,mg^{-1}_{cat}$ (with a FE of 14.1%), which maintained 83% (86% of the FE) of its initial value, demonstrating an excellent NRR stability. The SEM and TEM images (Figures S23 and S24) of $FeWS_x$@$FeWO_4$-2 after electrolysis were re-investigated, and the morphology of $FeWS_x$@$FeWO_4$-2 was maintained to be the same as that observed before electrolysis. Taking all the results together, we can conclude that $FeWS_x$@$FeWO_4$-2 is a robust catalyst for NRRs under ambient conditions.

Table S1 compares the performance of the $FeWS_x$@$FeWO_4$-2 catalyst with reported metallic sulfide-based materials for NRRs. Among the state-of-the-art metallic sulfide electrocatalysts for NRRs under ambient conditions,

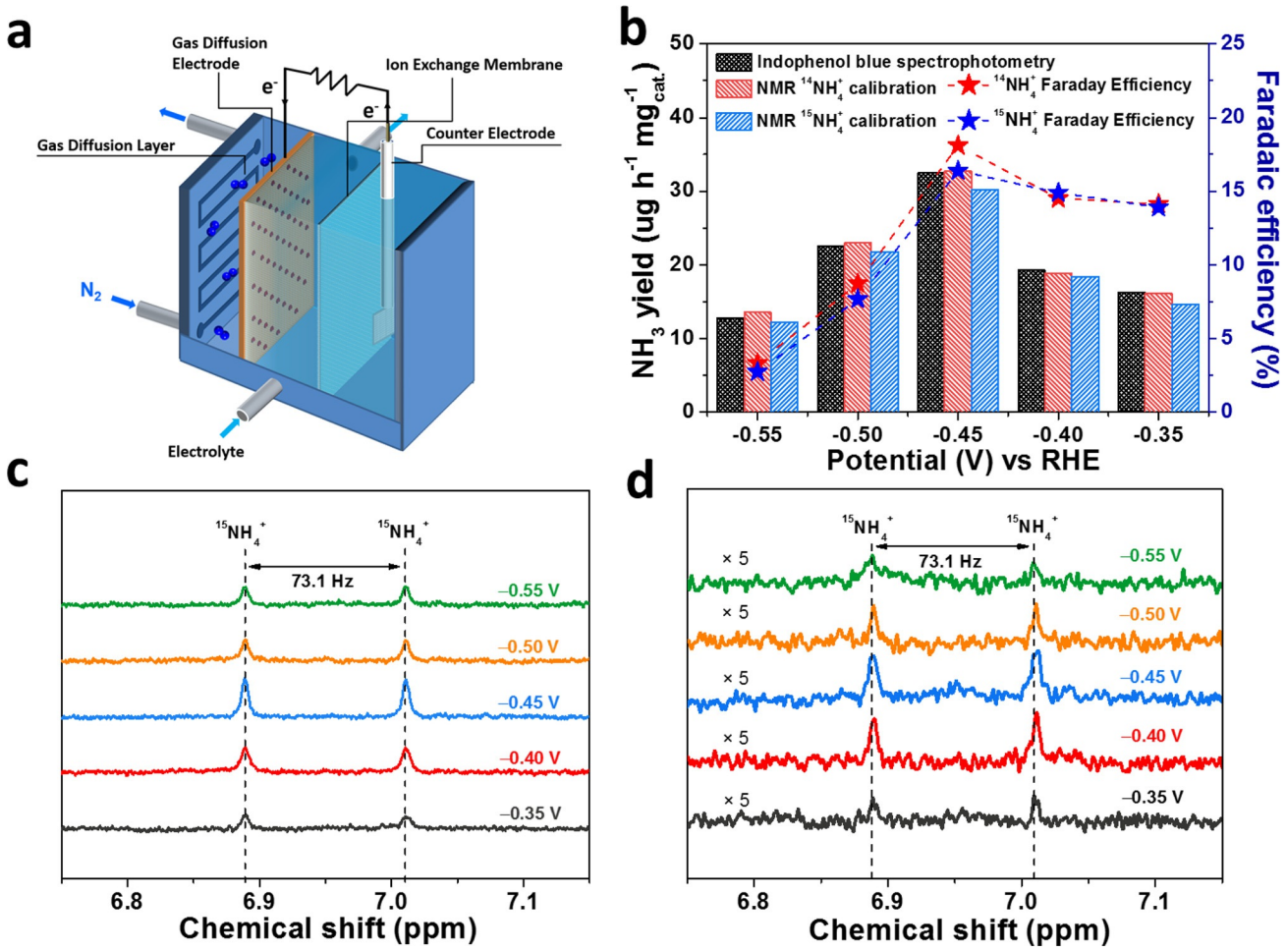

Figure 4. a) Schematic representation of the flow cell setup for the NRR. b) The yield of ammonia calibrated by three measurements and the Faraday efficiency of $^{15}N_2$ activity tests. ^{1}H-NMR spectra of $^{15}NH_4^+$ in c) electrolyte and d) gas absorption liquid (magnified five times) at corresponding potentials.

$FeWS_x$@$FeWO_4$-2 is superior to previously described catalysts in terms of r_{NH_3}, FE, and the optimum operating potential.

NRR Mechanism Study

As mentioned above, a comprehensive understanding of the catalytic mechanism plays a unique role in the development of efficient artificial NRR catalysts. In the current and early developmental state, NRR catalysts still suffer from sluggish kinetics accompanied by low N_2 adsorption and activation on the surface of the catalysts. As an outstanding catalyst for the electrocatalytic reduction of N_2, the reaction mechanism of $FeWS_x$@$FeWO_4$-2 is attractive.

The adsorption of N_2 on the catalyst surface was first investigated. After N_2 exposure, the samples were positioned in front of a shielded mass spectrometer and heated. As shown in the N_2 temperature-programmed desorption (N_2-TPD) spectra (Figure 5a), all samples exhibited a peak in the range of 50–175 °C, which can be attributed to the physical adsorption of N_2.[58] After vulcanization, new prominent TPD peaks with large adsorption areas corresponding to chemical adsorption can be observed around 265 °C for the $FeWS_x$@$FeWO_4$ samples. Meanwhile, the desorption peak of $FeWO_4$ for the chemically adsorbed N_2 shifts from 379 °C to 405 °C for $FeWS_x$@$FeWO_4$-2. This indicates that N_2 binding is stronger on the surface of the $FeWS_x$@$FeWO_4$ catalyst than on that of the $FeWO_4$ NPs; metal sulfur bonds are beneficial for N_2 adsorption. These N_2-TPD results coincided well with the measured NRR activities because $FeWS_x$@$FeWO_4$-2 exhibited the best catalytic performance.

Further insights into the activation process during the NRR of $FeWS_x$@$FeWO_4$-2 were explored by in situ Raman spectroscopy, which was used to probe the stretching vibrations of related intermediates formed on the surface of the catalyst (Figure S25). In the non-catalytic state, the multi-bonding and variations in bond angles were significant for the in situ Raman spectrum of the $FeWS_x$@$FeWO_4$-2 catalyst as compared to that of the dry catalyst (Figure S26), which was mainly attributed to the surface strain induced by atom reorientation after immersion into the KOH solution. As shown in Figure 5b, when the potential reached –0.4 V versus RHE, the vibration bands at 1119, 3207, 3288, and 3349 cm^{-1} could be observed, which were attributable to the stretching modes of N-N and N-H species.[59] Further, the intensities of these characteristic peaks increased with the rising potential.

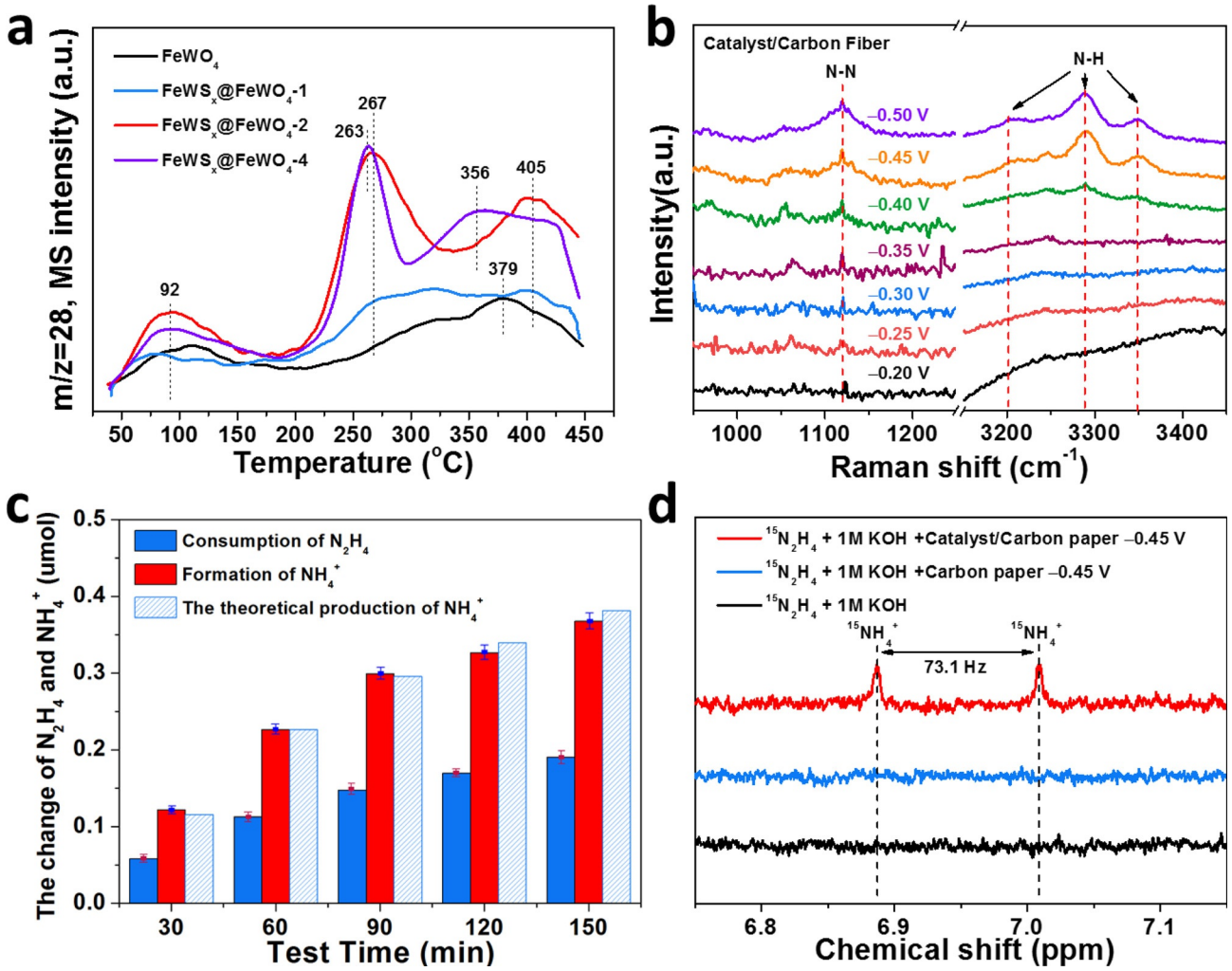

Figure 5. a) N_2-TPD profiles of $FeWO_4$ and $FeWS_x$@$FeWO_4$ catalysts. b) Electrochemical in situ Raman spectra of the surface of $FeWS_x$@$FeWO_4$-2 at different potentials. c) The consumption of hydrazine, the formation of ammonia, and theoretically calculated value of ammonia with different reaction times (−0.45 V, $FeWS_x$@$FeWO_4$-2 as the catalyst). d) ^{1}H-NMR spectra of $^{15}N_2H_4$ and blank experiments in 1 M KOH solution under various conditions.

In contrast, no characteristic Raman peaks were detected for the CFP substrate (Figure S27). These in situ Raman spectra indicated that intermediates with undissociated hydrazine structures are involved in the rate determing step (RDS) during the NRR for $FeWS_x$@$FeWO_4$-2. These undissociated hydrazine intermediates most likely serve as substrates for the RDS, thereby leading to the immediate consumption of the products obtained in the RDS, which is not easily observed.

In order to further confirm the presence of hydrazine species on the surface of $FeWS_x$@$FeWO_4$-2 during the NRR, the Raman spectra of CFP after adsorbing hydrazine hydrate were recorded. As shown in Figure S28, vibration bands at 1114, 3209, 3291, and 3347 cm^{-1} could be detected, which is consistent with the results of the in situ Raman spectra of $FeWS_x$@$FeWO_4$-2 confirming that the undissociated hydrazine species on the surface of $FeWS_x$@$FeWO_4$-2 are involved in the RDS of the NRR.

It is interesting that hydrazine could not be detected as an NRR product for $FeWS_x$@$FeWO_4$-2; however, intermediates with a hydrazine structure could be observed. Therefore, the electrocatalytic ability of hydrazine reduction for $FeWS_x$@$FeWO_4$-2 was investigated. O_2 and N_2 were carefully removed to avoid the influence of the NRR and hydrazine self-disproportionation. After electrolysis at −0.45 V versus RHE for different times, the concentrations of the remaining hydrazine in the electrolyte, the produced NH_3 in the electrolyte, and the gas absorption liquid were measured. As the electrolysis period increased (shown in Figure S29), the concentration of hydrazine gradually decreased, while the concentration of the produced NH_3 increased. Importantly, the amount of NH_3 produced was almost twice the amount of hydrazine consumed (Figure 5c), which indicated that the hydrazine decomposition process occurring on the surface of $FeWS_x$@$FeWO_4$-2 was actually the reduction of one hydrazine molecule into two molecules of NH_3 rather than a disproportionation reaction.[60,61] Meanwhile, isotope labeling experiments were also employed to prove the source of nitrogen for hydrazine reduction. As illustrated in Figure 5d, the ^{1}H-NMR spectra of the gas absorption liquid after electrolysis by $FeWS_x$@$FeWO_4$-2 using ^{15}N-hydrazine sulfate

($^{15}N_2H_6SO_4$) as the feeding material displayed a doublet (coupling constant of 73.1 Hz); however, $^{15}NH_4^+$ could not be detected in control experiments, which confirmed that the NH_3 production comes from the N–N bond cleavage reaction of hydrazine intermediates. In contrast, the hydrazine reduction on $FeWO_4$ surface can not correspond to the ammonia production by hydrazine homolysis (Figure S30); meanwhile, the corresponding peak of N-N species could not be observed in the in situ Raman (Figure S31), suggesting that the nitrogen reduction path on $FeWO_4$ surface is different from that of $FeWS_x$@$FeWO_4$-2; the appropriate vulcanization process plays an important role on the reduction path regulation.

As the undissociated hydrazine species on the surface of $FeWS_x$@$FeWO_4$-2 are involved in the RDS of the NRR. The rate of hydrazine decomposition was further calculated. The adsorption signal of hydrazine species on the surface of the catalyst was measured by Raman spectroscopy by adding different concentrations of hydrazine in the electrolytes (Figure 6a). The intensity of the characteristic N–N vibration bond at 1114 cm^{-1} could relatively reflect the adsorbed amount of hydrazine species on the surface of the catalyst. The intensity of the vibration bond increases with the concentration of the hydrazine solution. Importantly, when 1.0 mM hydrazine was added to the electrolyte, the Raman intensity (6.21) is comparable to signal intensity (6.26) under in situ electrochemical Raman conditions. Therefore, 1.0 mM hydrazine in the 1.0 M KOH was chosen as the electrolyte for the calculation of the rate for hydrazine reduction. Three independent electrolysis tests at −0.45 V were carried out, and the rate of hydrazine reduction was determined by the indophenol blue method (Figure 6b and Figure S32a,b). The average r_{NH3} for hydrazine reduction is 15.2 $ug\,h^{-1}mg^{-1}$ at −0.45 V, which is consistent to that of N_2 reduction (16.6 $ug\,h^{-1}mg^{-1}_{cat}$ at −0.45 V), suggesting that the reduction of undissociated hydrazine species on the surface of $FeWS_x$@$FeWO_4$-2 is the RDS for the electrochemical NRR. With higher concentrations of hydrazine (1.5 and 2.0 mM), there were no obvious changes that could be observed on the ammonia yield, indicating that the concentration of hydrazine had already reached to the upper limit of the catalytic conversion capacity (Figure S32c–f and Figure S33). The hydrazine reduction kinetics combining with the in situ Raman spectra results reveals that the reduction of the metal-hydrazine intermediate controls the reaction rate of the $FeWS_x$@$FeWO_4$-2 catalyst for the NRR.

Accordingly, alternate NRR hydrogenation mechanisms of on $FeWS_x$@$FeWO_4$-2 catalyst were proposed in Figure 6c. First, the Fe-W bimetallic sulfides chemisorbed nitrogen molecules in the side-on or terminal adsorption configurations. The adsorbed nitrogen molecules were activated and initiated the alternate hydrogenation processes by proton-coupled electron transfer. After the metal-hydrazine species formed on the surface of the catalyst as the crucial stable intermediates, further hydrogenation with the N–N bond breaking is the RDS of the $FeWS_x$@$FeWO_4$-2 catalyst for NRR. Eventually, the NH_3- species was formed and gradually desorbed from the catalyst surface, achieving the overall catalytic cycle.

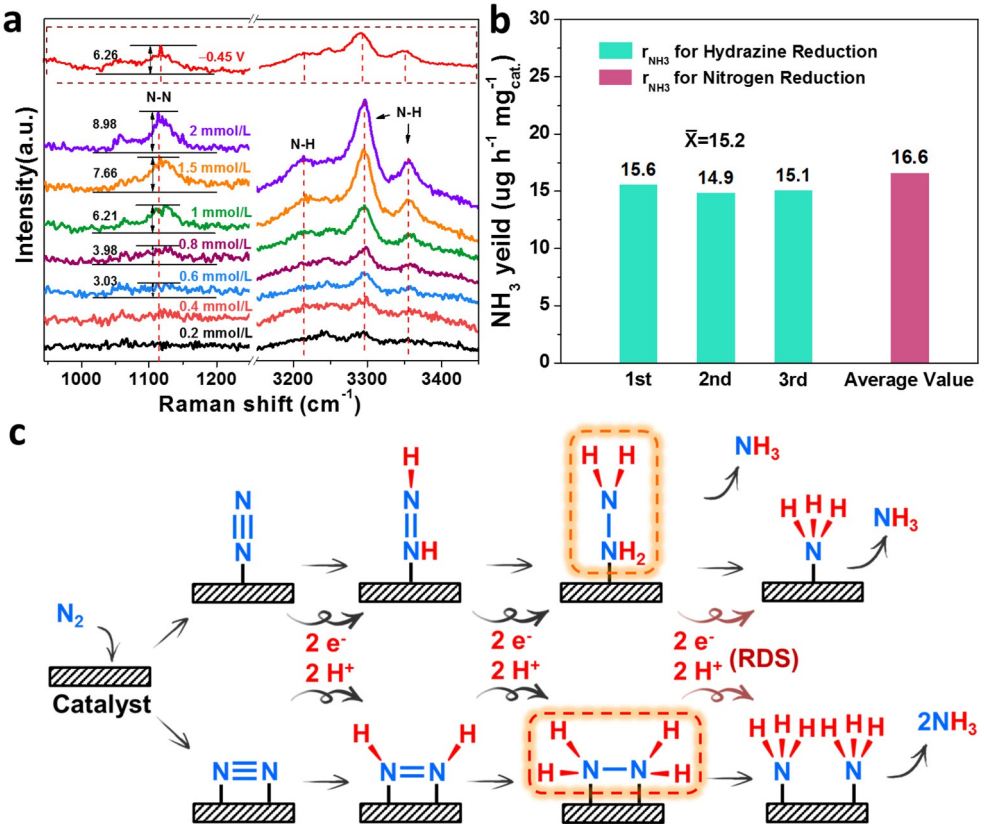

Figure 6. a) Electrochemical in situ Raman spectra of N_2H_4 adsorbed on the surface of $FeWS_x$@$FeWO_4$-2 in different concentrations of hydrazine solution (1 M KOH). b) The formation of ammonia with 1 mmol L^{-1} hydrazine solution (1 M KOH, −0.45 V, $FeWS_x$@$FeWO_4$-2 as catalyst). c) Schematic diagram of proposed pathways for N_2 reduction to NH_3 on $FeWS_x$@$FeWO_4$-2 catalyst.

Conclusion

In summary, an excellent bioinspired catalyst ($FeWS_x$@$FeWO_4$-2) for the electrocatalytic reduction of N_2 to ammonia was developed through sulfur substitution of the $FeWO_4$ NP surface. In a flow cell, the $FeWS_x$@$FeWO_4$-2 catalyst demonstrated an outstanding NH_3 production rate of 30.2 $ug\,h^{-1}mg^{-1}_{cat}$ with a Faraday efficiency of 16.4% at −0.45 V vs. RHE. Furthermore, the NH_3 yield rate in purified $^{15}N_2$-isotopic labeling experiments con-

firmed the NH_3 electroproduction. N_2-TPD results show that the metal-sulfur bonds introduced by appropriate vulcanization are beneficial for the chemical adsorption of N_2 on the surface of the catalysts. In-situ Raman spectra and the hydrazine reduction kinetics revealed that the efficient reduction of intermediates with metal-hydrazine structures plays an important role in the NRR rate for this catalyst, which might offer experimental and theoretical guidance for the investigation of the RDS for NRR catalysts. This work may provide new insights into the understanding of the reaction mechanism of NRR catalysts and facilitate the rational design of more advanced multimetallic sulfide materials for efficient electrochemical ammonia production.

Acknowledgements

This work was financially supported by the Fundamental Research Funds for the Central Universities (DUT19LK16), the National Natural Science Foundation of China (Grant No. 21120102036), the Swedish Research Council (2017-00935), and the K & AWallenberg Foundation (KAW 2016.0072).

Conflict of Interest

The authors declare no conflict of interest.

Keywords: bimetallic sulfide catalyst · hydrazine reduction · nitrogen reduction · rate-determining step · undissociated hydrazine intermediates

[1] B. M. Hoffman, D. Lukoyanov, Z.-Y. Yang, D. R. Dean, L. C. Seefeldt, *Chem. Rev.* **2014**, *114*, 4041 – 4062.
[2] D. E. Canfield, A. N. Glazer, P. G. Falkowski, *Science* **2010**, *330*, 192.
[3] C. Guo, J. Ran, A. Vasileff, S.-Z. Qiao, *Energy Environ. Sci.* **2018**, *11*, 45 – 56.
[4] J. Kibsgaard, J. K. Nørskov, I. Chorkendorff, *ACS Energy Lett.* **2019**, *4*, 2986 – 2988.
[5] A. J. Medford, M. C. Hatzell, *ACS Catal.* **2017**, *7*, 2624 – 2643.
[6] H. Zou, W. Rong, B. Long, Y. Ji, L. Duan, *ACS Catal.* **2019**, *9*, 10649 – 10655.
[7] J. S. Anderson, J. Rittle, J. C. Peters, *Nature* **2013**, *501*, 84 – 87.
[8] H.-P. Jia, E. A. Quadrelli, *Chem. Soc. Rev.* **2014**, *43*, 547 – 564.
[9] T. Kandemir, M. E. Schuster, A. Senyshyn, M. Behrens, R. Schlögl, *Angew. Chem. Int. Ed.* **2013**, *52*, 12723 – 12726; *Angew. Chem.* **2013**, *125*, 12955 – 12959.
[10] S. L. Foster, S. I. P. Bakovic, R. D. Duda, S. Maheshwari, R. D. Milton, S. D. Minteer, M. J. Janik, J. N. Renner, L. F. Greenlee, *Nat. Catal.* **2018**, *1*, 490 – 500.
[11] C. Tang, S.-Z. Qiao, *Chem. Soc. Rev.* **2019**, *48*, 3166 – 3180.
[12] P. J. Hill, L. R. Doyle, A. D. Crawford, W. K. Myers, A. E. Ashley, *J. Am. Chem. Soc.* **2016**, *138*, 13521 – 13524.
[13] J. B. Geri, J. P. Shanahan, N. K. Szymczak, *J. Am. Chem. Soc.* **2017**, *139*, 5952 – 5956.
[14] T. M. Buscagan, P. H. Oyala, J. C. Peters, *Angew. Chem. Int. Ed.* **2017**, *56*, 6921 – 6926; *Angew. Chem.* **2017**, *129*, 7025 – 7030.
[15] L. R. Doyle, A. J. Wooles, L. C. Jenkins, F. Tuna, E. J. L. McInnes, S. T. Liddle, *Angew. Chem. Int. Ed.* **2018**, *57*, 6314 – 6318; *Angew. Chem.* **2018**, *130*, 6422 – 6426.
[16] C. J. M. van der Ham, M. T. M. Koper, D. G. H. Hetterscheid, *Chem. Soc. Rev.* **2014**, *43*, 5183 – 5197.
[17] D. Bao, Q. Zhang, F.-L. Meng, H.-X. Zhong, M.-M. Shi, Y. Zhang, J.-M. Yan, Q. Jiang, X.-B. Zhang, *Adv. Mater.* **2017**, *29*, 1604799.
[18] L. Han, X. Liu, J. Chen, R. Lin, H. Liu, F. Lü, S. Bak, Z. Liang, S. Zhao, E. Stavitski, J. Luo, R. R. Adzic, H. L. Xin, *Angew. Chem. Int. Ed.* **2019**, *58*, 2321 – 2325; *Angew. Chem.* **2019**, *131*, 2343 – 2347.
[19] A. T. Thorhallsson, R. Bjornsson, *Inorg. Chem.* **2019**, *58*, 1886 – 1894.
[20] J. Rittle, J. C. Peters, *J. Am. Chem. Soc.* **2016**, *138*, 4243 – 4248.
[21] K. M. Lancaster, M. Roemelt, P. Ettenhuber, Y. Hu, M. W. Ribbe, F. Neese, U. Bergmann, S. DeBeer, *Science* **2011**, *334*, 974.
[22] R. D. Milton, R. Cai, S. Abdellaoui, D. Leech, A. L. De Lacey, M. Pita, S. D. Minteer, *Angew. Chem. Int. Ed.* **2017**, *56*, 2680 – 2683; *Angew. Chem.* **2017**, *129*, 2724 – 2727.
[23] R. N. F. Thorneley, R. R. Eady, D. J. Lowe, *Nature* **1978**, *272*, 557 – 558.
[24] X. Cui, C. Tang, Q. Zhang, *Adv. Energy Mater.* **2018**, *8*, 1800369.
[25] B. M. Barney, J. McClead, D. Lukoyanov, M. Laryukhin, T.-C. Yang, D. R. Dean, B. M. Hoffman, L. C. Seefeldt, *Biochemistry* **2007**, *46*, 6784 – 6794.
[26] B. M. Barney, D. Lukoyanov, T.-C. Yang, D. R. Dean, B. M. Hoffman, L. C. Seefeldt, *Proc. Natl. Acad. Sci. USA* **2006**, *103*, 17113.
[27] G. Ung, J. C. Peters, *Angew. Chem. Int. Ed.* **2015**, *54*, 532 – 535; *Angew. Chem.* **2015**, *127*, 542 – 545.
[28] N. Zhang, A. Jalil, D. Wu, S. Chen, Y. Liu, C. Gao, W. Ye, Z. Qi, H. Ju, C. Wang, X. Wu, L. Song, J. Zhu, Y. Xiong, *J. Am. Chem. Soc.* **2018**, *140*, 9434 – 9443.
[29] L. C. Seefeldt, B. M. Hoffman, D. R. Dean, *Annu. Rev. Biochem.* **2009**, *78*, 701 – 722.
[30] S. Rajagopal, D. Nataraj, O. Y. Khyzhun, Y. Djaoued, J. Robichaud, D. Mangalaraj, *J. Alloys Compd.* **2010**, *493*, 340 – 345.
[31] Y.-X. Zhou, H.-B. Yao, Q. Zhang, J.-Y. Gong, S.-J. Liu, S.-H. Yu, *Inorg. Chem.* **2009**, *48*, 1082 – 1090.
[32] R. Bhosale, S. Jain, C. P. Vinod, S. Kumar, S. Ogale, *ACS Appl. Mater. Interfaces* **2019**, *11*, 6174 – 6183.
[33] F. You, J. Wan, J. Qi, D. Mao, N. Yang, Q. Zhang, L. Gu, D. Wang, *Angew. Chem. Int. Ed.* **2020**, *59*, 721 – 724; *Angew. Chem.* **2020**, *132*, 731 – 734.
[34] B. Jansi Rani, G. Ravi, R. Yuvakkumar, M. Praveenkumar, S. Ravichandran, P. Muthu Mareeswaran, S. I. Hong, *ACS Omega* **2019**, *4*, 5241 – 5253.
[35] Y. D. Li, X. L. Li, R. R. He, J. Zhu, Z. X. Deng, *J. Am. Chem. Soc.* **2002**, *124*, 1411 – 1416.
[36] Y. Zhao, J. Wang, C. Ma, Y. Li, J. Shi, Z. Shao, *Chem. Eng. J.* **2019**, *378*, 122168.
[37] J. Qian, Z. Peng, D. Wu, X. Fu, *Mater. Lett.* **2014**, *122*, 86 – 89.
[38] G.-L. He, M.-J. Chen, Y.-Q. Liu, X. Li, Y.-J. Liu, Y.-H. Xu, *Appl. Surf. Sci.* **2015**, *351*, 474 – 479.
[39] O. El Jaroudi, E. Picquenard, A. Demortier, J.-P. Lelieur, J. Corset, *Inorg. Chem.* **2000**, *39*, 2593 – 2603.
[40] A. Matamoros-Veloza, O. Cespedes, B. R. G. Johnson, T. M. Stawski, U. Terranova, N. H. de Leeuw, L. G. Benning, *Nat. Commun.* **2018**, *9*, 3125.
[41] A. P. S. Gaur, S. Sahoo, J. F. Scott, R. S. Katiyar, *J. Phys. Chem. C* **2015**, *119*, 5146 – 5151.
[42] J. Li, C. Xiao, K. Wang, Y. Li, G. Zhang, *Environ. Sci. Technol.* **2019**, *53*, 11023 – 11030.
[43] S. Saftic, P. M. Fedorak, J. T. Andersson, *Environ. Sci. Technol.* **1992**, *26*, 1759 – 1764.
[44] K. C. Schreiber, *Anal. Chem.* **1949**, *21*, 1168 – 1172.
[45] E. E. Platero, M. P. Mentruit, *Catal. Lett.* **1994**, *30*, 31 – 39.

[46] D. A. Beattie, J. K. Chapelet, M. Gräfe, W. M. Skinner, E. Smith, *Environ. Sci. Technol.* **2008**, *42*, 9191 – 9196.
[47] S. Ramesh, T. F. Yuen, C. J. Shen, *Spectrochim. Acta Part A* **2008**, *69*, 670 – 675.
[48] T. Yamashita, P. Hayes, *Appl. Surf. Sci.* **2008**, *254*, 2441 – 2449.
[49] C. Wang, Q. Hu, Q. Zhang, J. Mei, S. Yang, *Ind. Eng. Chem. Res.* **2020**, *59*, 2745 – 2753.
[50] H. Y. F. Sim, J. R. T. Chen, C. S. L. Koh, H. K. Lee, X. Han, G. C. Phan-Quang, J. Y. Pang, C. L. Lay, S. Pedireddy, I. Y. Phang, E. K. L. Yeow, X. Y. Ling, *Angew. Chem. Int. Ed.* **2020**, *59*, 16997 – 17003; *Angew. Chem.* **2020**, *132*, 17145 – 17151.
[51] A. Nenning, A. K. Opitz, C. Rameshan, R. Rameshan, R. Blume, M. Hävecker, A. Knop-Gericke, G. Rupprechter, B. Klötzer, J. Fleig, *J. Phys. Chem. C* **2016**, *120*, 1461 – 1471.
[52] S. Z. Andersen, V. Čolić, S. Yang, J. A. Schwalbe, A. C. Nielander, J. M. McEnaney, K. Enemark-Rasmussen, J. G. Baker, A. R. Singh, B. A. Rohr, M. J. Statt, S. J. Blair, S. Mezzavilla, J. Kibsgaard, P. C. K. Vesborg, M. Cargnello, S. F. Bent, T. F. Jaramillo, I. E. L. Stephens, J. K. Nørskov, I. Chorkendorff, *Nature* **2019**, *570*, 504 – 508.
[53] Y. Zhao, R. Shi, X. Bian, C. Zhou, Y. Zhao, S. Zhang, F. Wu, G. I. N. Waterhouse, L.-Z. Wu, C.-H. Tung, T. Zhang, *Adv. Sci.* **2019**, *6*, 1802109.
[54] M.-M. Shi, D. Bao, B.-R. Wulan, Y.-H. Li, Y.-F. Zhang, J.-M. Yan, Q. Jiang, *Adv. Mater.* **2017**, *29*, 1606550.
[55] H. Zou, W. Rong, S. Wei, Y. Ji, L. Duan, *Proc. Natl. Acad. Sci. USA* **2020**, *117*, 29462 – 29468.
[56] C. Chen, X. Zhu, X. Wen, Y. Zhou, L. Zhou, H. Li, L. Tao, Q. Li, S. Du, T. Liu, D. Yan, C. Xie, Y. Zou, Y. Wang, R. Chen, J. Huo, Y. Li, J. Cheng, H. Su, X. Zhao, W. Cheng, Q. Liu, H. Lin, J. Luo, J. Chen, M. Dong, K. Cheng, C. Li, S. Wang, *Nat. Chem.* **2020**, *12*, 717 – 724.
[57] B. H. R. Suryanto, H.-L. Du, D. Wang, J. Chen, A. N. Simonov, D. R. MacFarlane, *Nat. Catal.* **2019**, *2*, 290 – 296.
[58] Y. Yang, L. Zhang, Z. Hu, Y. Zheng, C. Tang, P. Chen, R. Wang, K. Qiu, J. Mao, T. Ling, S.-Z. Qiao, *Angew. Chem. Int. Ed.* **2020**, *59*, 4525 – 4531; *Angew. Chem.* **2020**, *132*, 4555 – 4561.
[59] R. Chellappa, D. Dattelbaum, L. Daemen, Z. Liu, *J. Phys. Conf. Ser.* **2014**, *500*, 052008.
[60] D. V. Yandulov, R. R. Schrock, *Inorg. Chem.* **2005**, *44*, 1103 – 1117.
[61] D. V. Yandulov, R. R. Schrock, *J. Am. Chem. Soc.* **2002**, *124*, 6252 – 6253.

Manuscript received: April 9, 2021
Accepted manuscript online: July 10, 2021
Version of record online: August 6, 2021

